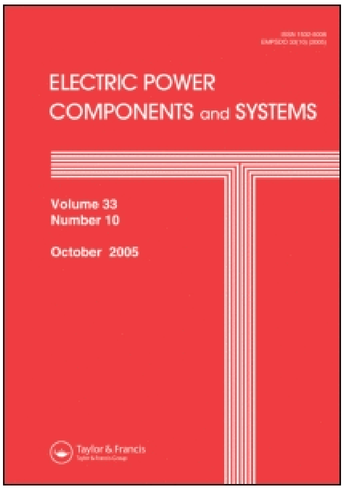

Electric Power Components and Systems
Publication details, including instructions for authors and subscription information:
http://www.informaworld.com/smpp/title~content=t713399721

Adjustable-speed Unsymmetrical Two-phase Induction Motor Drive for Photovoltaic Powered Air Conditioners

Naser M. B. Abdel-Rahim[a]
[a] Electrical Engineering Department, Benha University, Cairo, Egypt

Online publication date: 27 May 2010

To cite this Article Abdel-Rahim, Naser M. B.(2010) 'Adjustable-speed Unsymmetrical Two-phase Induction Motor Drive for Photovoltaic Powered Air Conditioners', Electric Power Components and Systems, 38: 8, 865 — 880
To link to this Article: DOI: 10.1080/15325000903571186
URL: http://dx.doi.org/10.1080/15325000903571186

Electric Power Components and Systems, 38:865–880, 2010

ISSN: 1532-5008 print/1532-5016 online
DOI: 10.1080/15325000903571186

Adjustable-speed Unsymmetrical Two-phase Induction Motor Drive for Photovoltaic Powered Air Conditioners

NASER M. B. ABDEL-RAHIM[1]

[1]Electrical Engineering Department, Benha University, Cairo, Egypt

Abstract *This article proposes a novel application of adjustable-speed one-phase induction motors in air conditioners powered by photovoltaic arrays. Employing the slip-frequency control scheme, an off-the-shelf one-phase induction motor is operated as an unsymmetrical two-phase induction motor. Maintaining certain control conditions, the unsymmetrical two-phase induction motor is made to behave like a symmetrical two-phase induction motor. This has the advantage of increasing the motor efficiency and reducing the torque pulsations inherent to unsymmetrical two-phase induction motors. The proposed control scheme reduces both initial and running costs of the proposed photovoltaic system. Initial cost is cut down by reducing the required size of the photovoltaic array through (i) limiting the motor current during both transient and dynamic phases of operation, (ii) extracting maximum power from the photovoltaic array under various climate conditions by operating the photovoltaic array on the maximum power line, and (iii) dispensing with the need for specially designed two-phase induction motors. Reduction in the running cost of the photovoltaic system is achieved by enhancing the motor efficiency through eliminating the backward component of the air gap flux. The article outlines a procedure for sizing the photovoltaic arrays. Simulation results of the system behavior during transient and dynamic phases confirm the capability of the proposed scheme.*

Keywords photovoltaic applications, slip frequency control, unsymmetrical two-phase induction motors, maximum power point tracker, photovoltaic-powered air conditioners

1. Introduction

Air conditioners powered by a conventional AC supply commonly use one-phase induction motors (IMs) despite their inferior performance when compared to that of poly-phase IMs. One-phase IMs primarily suffer from zero starting torque, higher torque pulsations, bigger frame size, and inherently lower efficiency. To overcome such shortcomings, and to cope with the shift from conventional energy sources to environmentally friendly renewable energy sources, this article proposes to operate a one-phase IM as a symmetrical two-phase IM fed from a photovoltaic (PV) array. This mode of operation has numerous advantages. First, it rids the motor of the backward component of the air gap flux, hence decreasing the motor iron losses, leading to higher motor efficiency. Second, it endows the "one-phase" IM with the merits of poly-phase motors such as non-zero starting torque,

Received 10 October 2008; accepted 29 October 2009.
Address correspondence to Naser M. B. Abdel-Rahim, Electrical Engineering Department, Faculty of Engineering at Shoubra, Benha University, 108 Shoubra street, Cairo, 11240, Egypt. E-mail: nabdelrahim@gmail.com

low torque pulsations, and higher output power for the same motor frame size [1]. Third, it departs from conventional energy sources that have become less favorable with the ongoing increase in fuel prices as well as the growing awareness of the environmental impact of fossil fuel consumption. The proposed system is fed by solar energy directly converted into electricity using PV panels, a trend which has shown rapid growth [2, 3]. For instance, the annual world PV panel production in 2005 presented a growth of 45% over that of 2004 [4]. In fact, the use of PV energy in residential applications has been the focus of a considerable body of research [5–11]. Yet, PV systems have not been employed to their full potential due to their deterring high initial cost.

Thus, this work proposes several techniques that can help reduce both the initial and running costs of the PV system. Initial cost is cut down by reducing the required size of the PV array through (i) limiting the motor current during both transient and dynamic phases of operation, (ii) extracting maximum power from the PV array under various climate conditions by operating the PV array on the maximum power line, and (iii) dispensing with the need for specially designed two-phase IMs, since two-phase IM merits are realized through manipulating the operation of a one-phase IM. This has the added advantage of reducing the motor losses, which results in the reduction of the running cost of the PV system, which, in turn, further enhances the overall system efficiency. The article outlines a procedure for sizing the PV arrays. Simulation results of the system behavior during transient and dynamic phases confirm the capability of the proposed scheme.

2. Operation of One-phase IM as Symmetrical Two-phase IM

In order to make an off-the-shelf one-phase IM behave like a symmetrical two-phase IM, the terminals of the main and auxiliary windings of the one-phase IM are disconnected from each other. Then, these two unsymmetrical windings are independently excited such that the following relationship is always obeyed [12]

$$I_2 = jaI_1, \tag{1}$$

where I_1 is the current in the main winding, I_2 is the current in the auxiliary winding, and a is the turns ratio of the main to the auxiliary windings (N_1/N_2).

With Eq. (1) observed throughout all operating conditions, an equivalent circuit of the one-phase IM when operated as symmetrical two-phase IM was derived in [13] and is shown in Figure 1, where

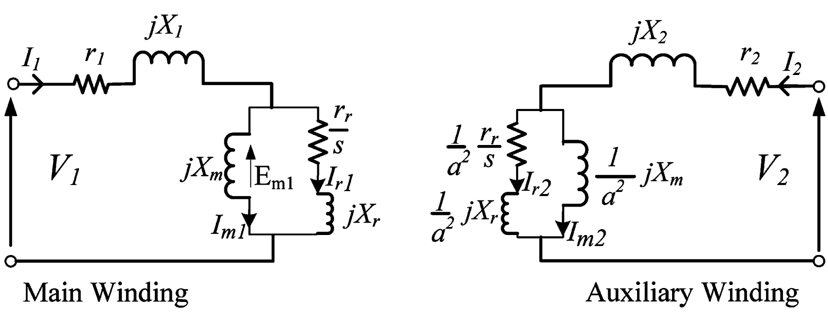

Figure 1. Equivalent circuit of the unsymmetrical two-phase IM when operated in the symmetrical two-phase mode.

r_1 and r_2 are the resistances of the main and auxiliary windings, respectively;
X_1 and X_2 are the leakage reactances of the main and auxiliary windings, respectively;
r_r is the rotor resistance (referred to the main winding);
X_r is the rotor leakage reactance (referred to the main winding);
X_m is the magnetizing reactance;
I_{m1} and I_{m2} are the magnetizing currents of the main and auxiliary windings, respectively; and
s is the rotor slip.

3. Variable-speed Operation

Variable-speed control of the one-phase IM operated as a symmetrical two-phase IM is carried out using the slip-frequency control (SFC) scheme. The essence of the SFC scheme is to maintain the motor air gap flux at its rated value at various operating conditions. Referring to Figure 1, the magnetizing current of the main winding can be written as

$$I_{m1} = I_1 \frac{r_r + jsX_r}{r_r + js(X_m + X_r)}, \tag{2}$$

where

$$s = \frac{\omega_s - \omega_m}{\omega_s} = \frac{\omega_{sL}}{\omega_s}, \tag{3}$$

and ω_m is the actual motor speed (rad/sec), ω_{sL} is the rotor slip frequency (rad/sec), and ω_s is the synchronous frequency (rad/sec).

The magnitude of the current in the main windings, $|I_1|$, in terms of the rotor slip frequency and the motor parameters is obtained by substituting Eq. (3) into Eq. (2) and rearranging:

$$|I_1| = |I_{m1}| \sqrt{\frac{r_r^2 + \omega_{sL}^2 (L_m + L_{lr})^2}{r_r^2 + \omega_{sL}^2 L_{lr}^2}}. \tag{4}$$

In order to keep the air gap flux of the main windings fixed at its rated value for various rotor slips, $|I_{m1}|$ in Eq. (4) is kept constant at its full-load magnitude ($|I_{m1}|_{f.l.}$). Referring to Figure 1, $|I_{m2}|$, $|I_2|$, and $|I_{r2}|$ are given by

$$|I_{m2}| = a \times |I_{m1}|, \tag{5}$$

$$|I_2| = a \times |I_1|, \tag{6}$$

$$|I_{r2}| = a \times |I_{r1}|. \tag{7}$$

With the magnitudes of the motor magnetizing currents kept fixed at their rated values for various operating conditions, the two-phase IM never enters saturation, and the motor is resolved into an equivalent separately excited DC motor in terms of its speed of response, not in terms of decoupling the flux and torque channels [14].

For the one-phase motor parameters given in Appendix A, it was shown that, at the same value of steady-state slip, the motor produces 23.4% more power when operated in the two-phase mode of operation [1]. In other words, for a 1.5-hp one-phase IM operated in the two-phase mode, the new motor output power becomes

$$P_{out} = 1.234 \times 1.5 = 1.851 \text{ hp} = 1.3801 \text{ kW}. \tag{8}$$

Referring to Figure 1, the motor output power can be written as

$$P_{out} = |I_{r1}^2| \frac{r_r}{s}(1-s) + |I_{r2}^2| \frac{r_r}{a^2 s}(1-s) = 1380.9 \text{ W}. \tag{9}$$

For a steady-state slip of 5%, and substituting Eq. (7) into Eq. (9), the full-load value of $|I_{r1}|$ is calculated as

$$|I_{r1}|_{f.l.} = 4.2 \text{ A}. \tag{10}$$

Referring to Figure 1, the rated value of the magnetizing current of the main winding ($|I_{m1}|_{f.l.}$) can be obtained as

$$|I_{m1}|_{f.l.} = \frac{|(E_{m1})_{f.l.}|}{jX_m} = \frac{|(I_{r1})_{f.l.}| \dfrac{r_r}{s_{f.l.}}}{jX_m}. \tag{11}$$

Equation (11) is obtained by neglecting the voltage drop across X_r. Using the motor parameters given in Appendix A, $|I_{m1}|_{f.l.}$ is calculated as 1.7 A. Substituting Eq. (11) into Eq. (4) gives

$$|I_1| = 1.7\sqrt{\frac{r_r^2 + \omega_{sL}^2 (L_m + L_{lr})^2}{r_r^2 + \omega_{sL}^2 L_{lr}^2}}. \tag{12}$$

Once again, the current in the auxiliary winding is given in terms of the current in the main winding by Eq. (6). The relationship between the magnitude of the current in the main winding and the rotor slip is shown in Figure 2. The figure shows that a limit can be set on the maximum value of the main/auxiliary winding currents by limiting the maximum excursion of the rotor slip frequency ω_{sL} to a predetermined value. Limiting the maximum value of both the main and auxiliary windings currents has the advantage of reducing the current ratings of the power inverter switching devices, as well as reducing the number of the required PV panels, hence, reducing the overall system cost. In this work, the maximum value of the currents in the main/auxiliary winding is set to 1.5 of their full-load values.

4. The Proposed Scheme

Figure 3 shows the layout of the proposed system. It consists of PV panels (array) in series with a second-order LC filter. The filter capacitor is used to provide a by-pass for the harmonics generated by the switching inverter. The filter inductor further smoothes the output current of the PV array, which results in better quality DC voltage across the capacitor. Two one-phase full-bridge inverters are used to operate the one-phase IM in the two-phase mode of operation. The two-phase IM drives the compressor of the air conditioner. Referring to Figure 3, the principle of operation of the control scheme is as follows.

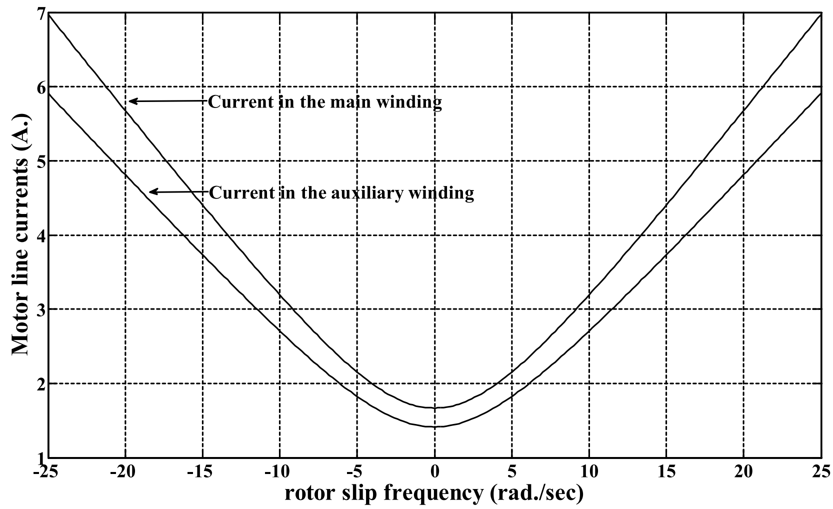

Figure 2. Relationship between the main and auxiliary windings currents and the rotor slip frequency.

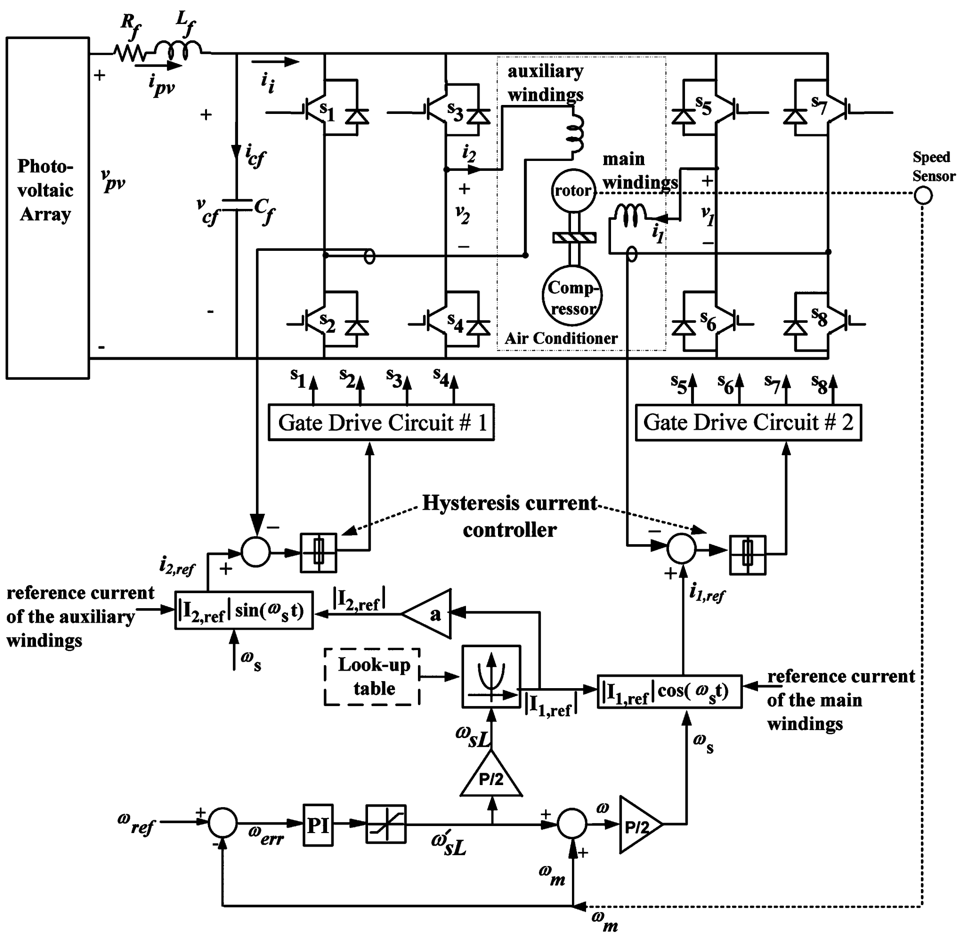

Figure 3. Proposed drive system.

First, the actual motor speed ω_m is compared with its reference signal ω_{ref} to produce the slip frequency ω_{err}. ω_{err} is conditioned by the proportional-integral (PI) regulator and then passed through a limiter that limits the excursion of the slip frequency to produce ω'_{sL}. The value of ω'_{sL} is first multiplied by the number of motor pole pairs and is then used along with the look-up table shown in Figure 2 to obtain the magnitude of the commanding signal of the current in the main winding, $|I_{1,ref}|$. The magnitude of the commanding signal of the current in the auxiliary winding, $|I_{2,ref}|$, is obtained by multiplying $|I_{1,ref}|$ by the ratio "a."

Second, ω'_{sL} is added to the motor actual speed ω_m to produce ω. ω is then multiplied by the number of motor pole pairs to produce the inverter output frequency, which is the motor synchronous frequency ω_s. The values of ω_s along with $|I_{1,ref}|$ and $|I_{2,ref}|$ are used to generate the reference waveforms of the currents in the main winding $i_{1,ref}$ and auxiliary winding $i_{2,ref}$, respectively.

Finally, the actual stator currents are compared with their respective reference waveforms, $i_{1,ref}$ and $i_{2,ref}$, in a hysteresis current comparator. The output of the hysteresis comparator of the auxiliary winding is used to control the inverter switching devices S1 to S4 while the output of the hysteresis current controller of the main winding is used to control the inverter switches S5 to S8, such that the error between the actual motor speed and the reference speed is reduced.

5. Sizing the PV Array

This section determines the rating of the PV array. For a motor output power equal to 1380.9 W (refer to Eq. (8)) and motor parameters given in Appendix A, the RMS values of the motor rated terminal voltages are calculated using the motor equivalent circuit shown in Figure 1 as

$$V_{main} = 184.5 \text{ V(RMS)}, \tag{13}$$

$$V_{aux} = 220 \text{ V(RMS)}. \tag{14}$$

The output voltage of the PV array should be high enough to provide a fundamental component at the inverter output voltage that is equal to the motor rated voltage at its full load conditions. Thus, the magnitude of the DC bus voltage is chosen to be equal to the peak of V_{aux}, *i.e.*,

$$v_{pv} = 220 \times \sqrt{2} = 311 \text{ V}. \tag{15}$$

Using Siemens solar module (SP75, Siemens Solar Industries, Camarillo, California, USA; Appendix B), the module output voltage (V_{om}) at which the maximum output power can be extracted from the PV module, is 17 V [15]. Thus, the number of required series-connected modules of the PV array is given by

$$N_s = \frac{v_{pv}}{V_{om}} = \frac{311}{17} = 18.29, \tag{16}$$

where v_{pv} is the total output voltage of the PV array. Hence, the number of series-connected modules is chosen to be 19. At 100% solar insolation, the PV array should be capable of supplying the motor full-load current with the output voltage of the PV array,

v_{pv}, set at its maximum power point (MPP). With the motor reactive power provided by the inverter, the PV array has to supply only the active power required by the motor [16]. Thus, for a motor output of 1380.9 W, and an overall motor efficiency of 84% [1], the motor input active power is given by

$$P_{ac} = \frac{1380.9}{0.84} = 1643.9 \text{ W}. \tag{17}$$

Assuming inverter efficiency η_{inv} of 90%, the power required on the DC side of the inverter becomes

$$P_{dc} = \frac{P_{ac}}{\eta_{inv}} = \frac{1643.9}{0.9} = 1826.6. \tag{18}$$

The DC power supplied by the PV array P_{pv} is given by

$$P_{pv} = I_{pv} V_{pv} = P_{dc}. \tag{19}$$

The required output current of the PV array I_{pv} is obtained from Eqs. (18) and (19) as

$$I_{pv} = \frac{P_{dc}}{V_{pv}} = \frac{1826.6}{311} = 5.9 \text{ A}. \tag{20}$$

Assuming a peak solar hour (PSH) of 5.5 and a duty ratio of the air conditioner of one-third (*i.e.*, operating 8 hr/day), the required output current of the PV array is given by [17]

$$I_{pv}|_{req} = \frac{8 \times I_{pv}}{PSH} = \frac{8 \times 5.9}{5.5} = 8.5 \text{ A}. \tag{21}$$

The number of parallel-connected strings required to supply the load current is given by

$$N_p = SF \frac{I_{pv}|_{req}}{I_{\text{mod}}}, \tag{22}$$

where *SF* is a sizing factor that is used to oversize the current available from the PV array and I_{mod} is the module output current at maximum output power. With $I_{mod} = 4.4$ Amp, $N_p = 1.94$. Thus, the number of parallel-connected modules is chosen to be two. This gives an *SF* of 1.04, *i.e.*, an effective oversizing of approximately 4%.

6. Simulation Results

The system shown in Figure 3 was simulated using Matlab/Simulink [18]. The load torque presented by a compressor that supplies a constant pressure system may slightly vary with a variation of speed [19]. In the present work, the slight variation of load torque with respect to speed is neglected, and the load torque is, therefore, considered constant. The motor dynamic model was integrated with a PV array model [17] to simulate the overall system.

The system was first started with the two-phase IM disconnected and with the LC filter $(L_f - C_f)$ as the only load connected to the PV array. This allows the voltage across the DC filter capacitor to build up quickly and reduce the overall transient time of the system. This situation is maintained until the value of the voltage across the DC filter capacitor reaches the peak value of the motor rated voltage $220\sqrt{2} = 311$ V; then, the fully loaded two-phase IM is switched ON.

Figure 4 shows the simulation results of various variables of the proposed system at 100% insolation. Figure 4(a) shows that the PV array output current is close to its maximum (short-circuit) value during the first 0.37 sec of operation to provide for the large value of the current required to charge up the DC filter capacitor. The figure also shows that once the motor is switched ON, the PV array output current (i_{pv}) increases to meet the power demand by the fully loaded motor. The PV array output current reaches its steady-state value of 4.0 Amp at approximately 4.2 sec. Figure 4(b) shows that the control scheme is capable of driving the motor at the command speed (100 rad/sec) with a steady-state error of −0.43% with controller parameters $K_p = 4.0$ and $K_i = 2.0$. Figure 4 shows that the system takes 4.2 sec to reach its steady-state operating conditions.

Figure 5 shows the simulation results of the currents in the main and auxiliary windings of the two-phase IM at 100% insolation. Figures 5(a) and 5(b) show that the scheme is capable of limiting the stator currents to a maximum of 1.5 times their respective steady-state full-load values. Limiting the motor starting current, however, results in a slightly prolonged startup time. Nevertheless, successful starting of the motor is accomplished. Figures 5(c) and 5(d) show that the motor currents are sinusoidal with reduced harmonic content. These harmonics will be filtered out and their effects are further minimized through the motor leakage inductance.

Figure 6 shows the transient, dynamic, and steady-state behavior of the system at 100% insolation. Figures 6(a) and 6(b) show the motor currents during transients,

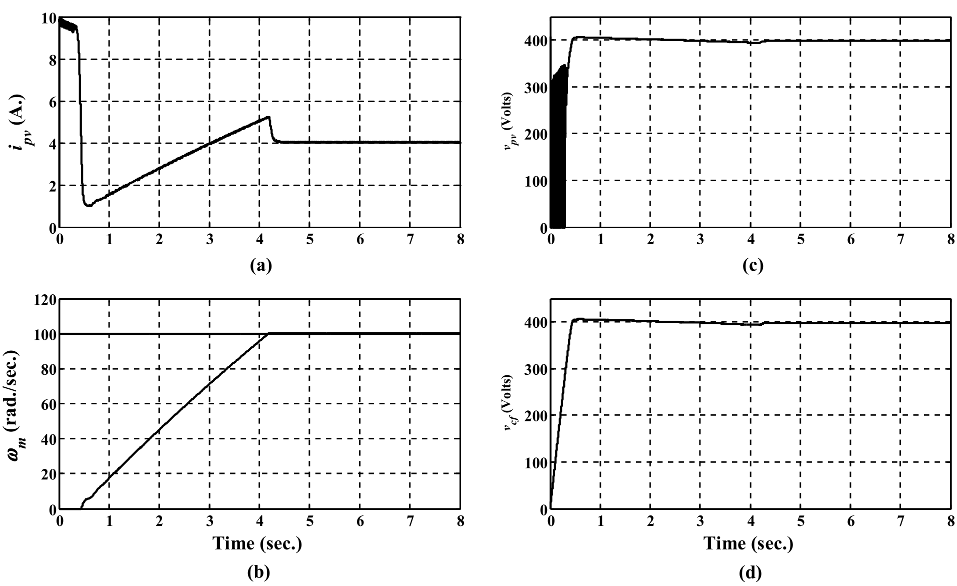

Figure 4. Simulation results of the transient and steady-state behavior of the proposed system at 100% insolation: (a) PV array output current, (b) motor speed, (c) PV array output voltage, and (d) DC filter capacitor voltage.

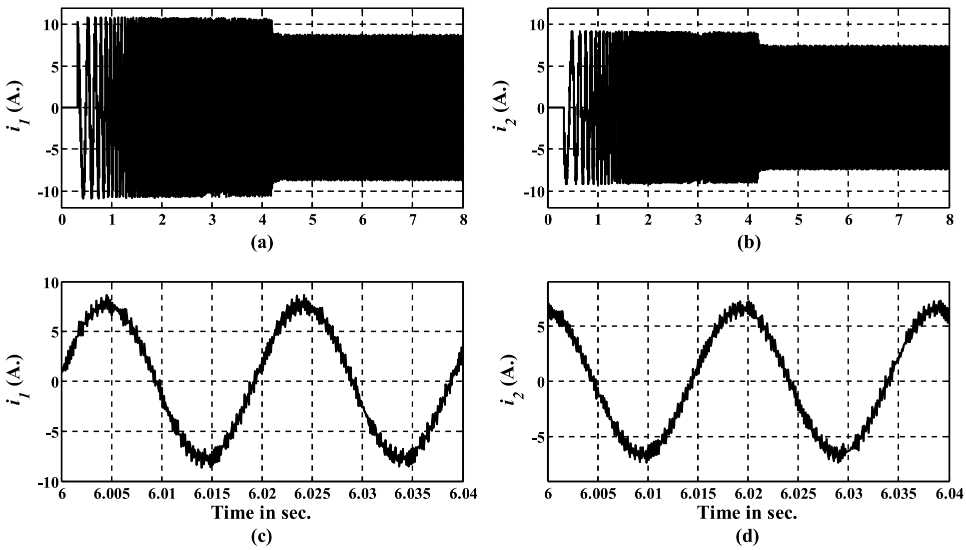

Figure 5. Simulation results of the transient and steady-state behavior of the proposed system at 100% insolation: (a) current in the main winding, (b) current in the auxiliary winding, (c) magnified view of (a), and (d) magnified view (b).

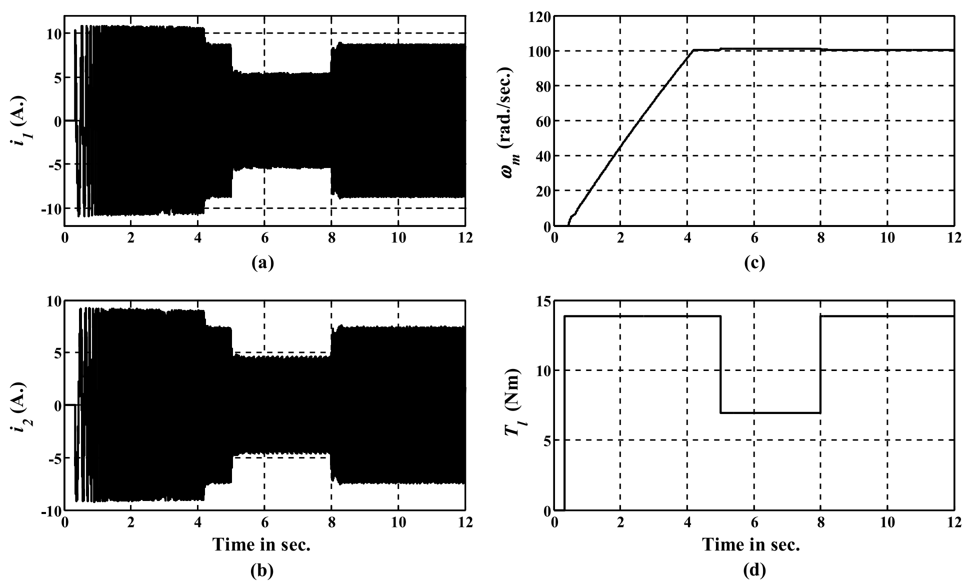

Figure 6. Simulation results of transient, dynamic, and steady-state behavior of the motor currents and motor speed for 50% step changes in the load at 100% insolation: (a) current in the main winding, (b) current in the auxiliary winding, (c) motor speed, and (d) load torque variation.

steady-state, and during 50% step reduction of load torque. At $t = 5.0$ sec, 50% reduction of the load torque takes place, and later, at $t = 8.0$ sec, the full-load torque is restored (see Figure 6(d)). Figures 6(a) and 6(b) depict the effect of these torque changes on the motor currents. Figure 6(c) shows that during the 50% step change of load torque, there is a slight increase in the motor speed. However, good speed regulation is still in effect during these sudden load changes (speed error of -1.3%).

Figure 7 shows the PV array output current (i_{pv}), voltage (v_{pv}), and DC filter capacitor voltage (v_{cf}), during transient, full-load, and half-load operation at 100% insolation. The load torque variation, shown in Figure 7(b), is repeated here for convenience. Figure 7(a) shows that at starting, the level of i_{pv} is very close to the value of the short-circuit current of the PV array. The figure shows that a 50% step reduction in the load torque results in a 50% reduction in i_{pv} when compared with its full-load value. i_{pv} regains its full-load value at $t = 8.0$ sec, where the motor torque is once again brought to its full-load value.

Figures 8 and 9 show the behavior of the system at 60% solar insolation. Due to the reduction in the power available to the PV array, the DC capacitor voltage takes slightly longer time (0.54 sec) to reach 311 V. The figures confirm that the system is capable of starting and running the motor with full load at as low as 40% reduction of solar insolation.

Figures 10 and 11 show the system behavior at 30% solar insolation. Due to further reduction in the power available from the PV array, the DC filter capacitor voltage takes longer time (0.81 sec) to reach 311 V. The figures show that the system is still capable of starting and running the motor with full load but at reduced motor speed (70 rad/sec).

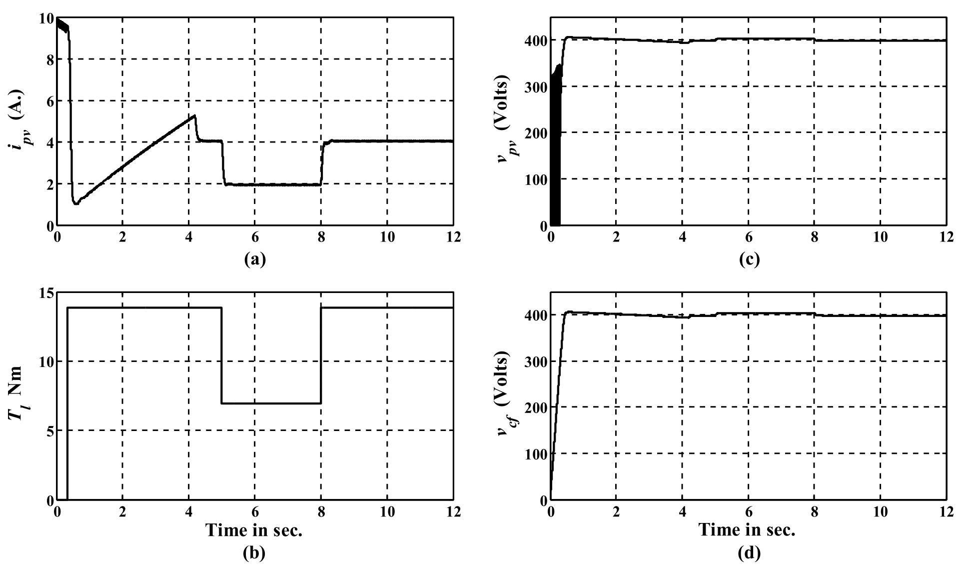

Figure 7. Simulation results of transient, dynamic, and steady-state behavior of the PV array output voltage and current and the voltage of the DC filter capacitor for 50% step change in the load at 100% insolation: (a) PV array output current, (b) load torque variation, (c) PV array output voltage, and (d) capacitor voltage.

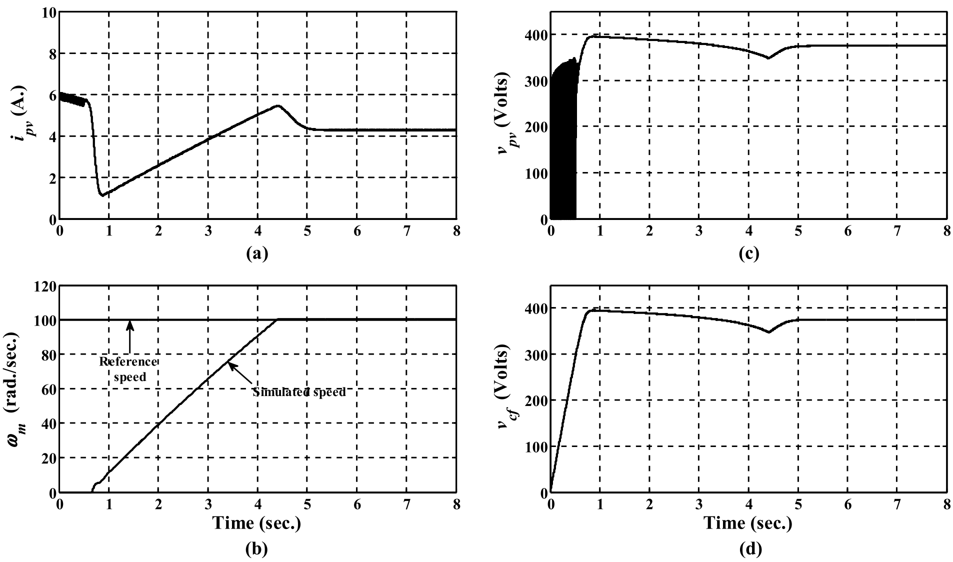

Figure 8. Simulation results of transient and steady-state behavior of the PV array output voltage, current, and the voltage of the DC filter capacitor at 60% insolation: (a) PV array output current, (b) motor speed, (c) PV array output voltage, and (d) DC filter capacitor voltage.

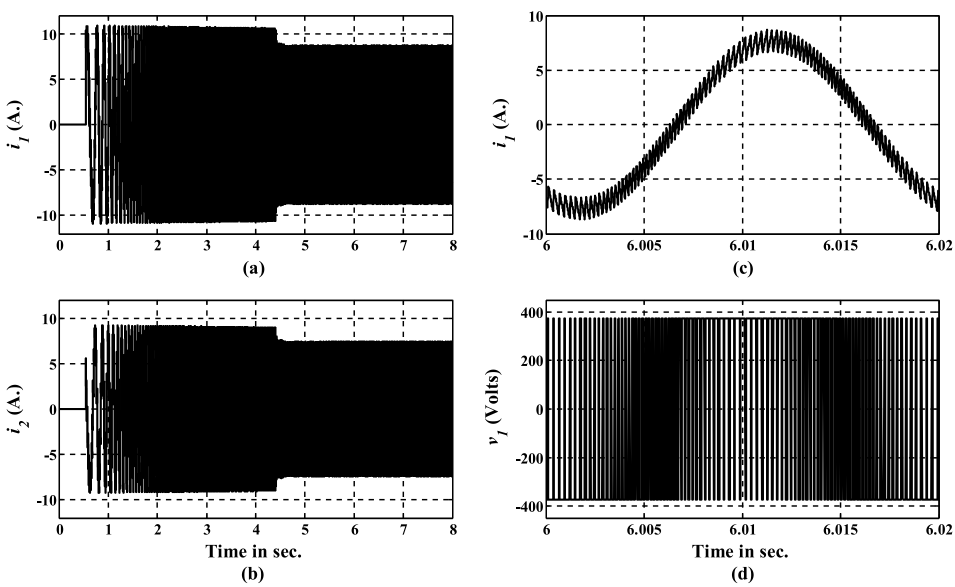

Figure 9. Simulation results of transient and steady-state behavior of the PV array output voltage and current and the voltage of the DC filter capacitor at 60% insolation: (a) current in the main winding, (b) current in the auxiliary winding, (c) magnified view of (a), and (d) magnified view of the main winding voltage.

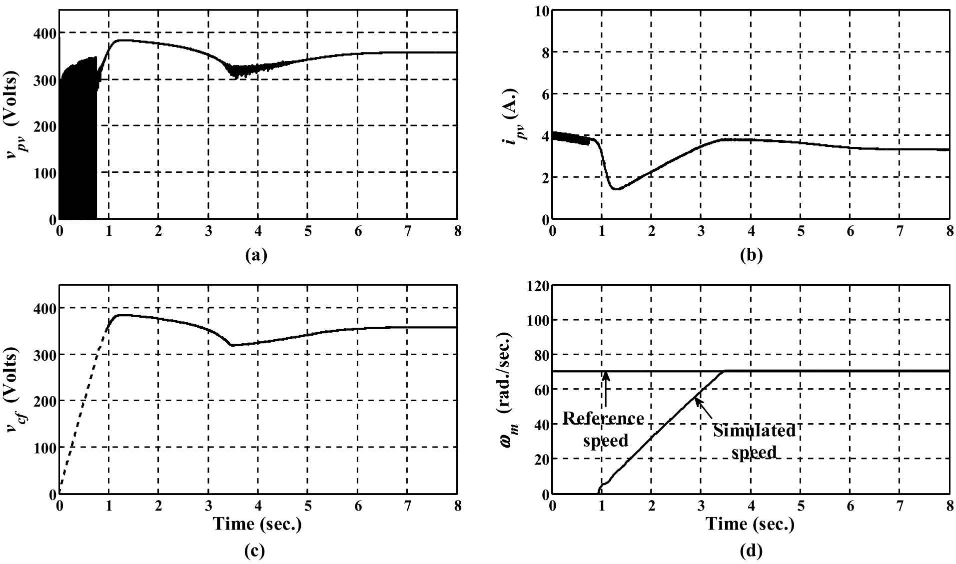

Figure 10. Simulation results of transient and steady-state behavior of the PV array output voltage and current, the voltage of the DC filter capacitor, and motor speed at 30% insolation: (a) PV array output voltage, (b) PV array output current, (c) DC filter capacitor voltage, and (d) motor speed.

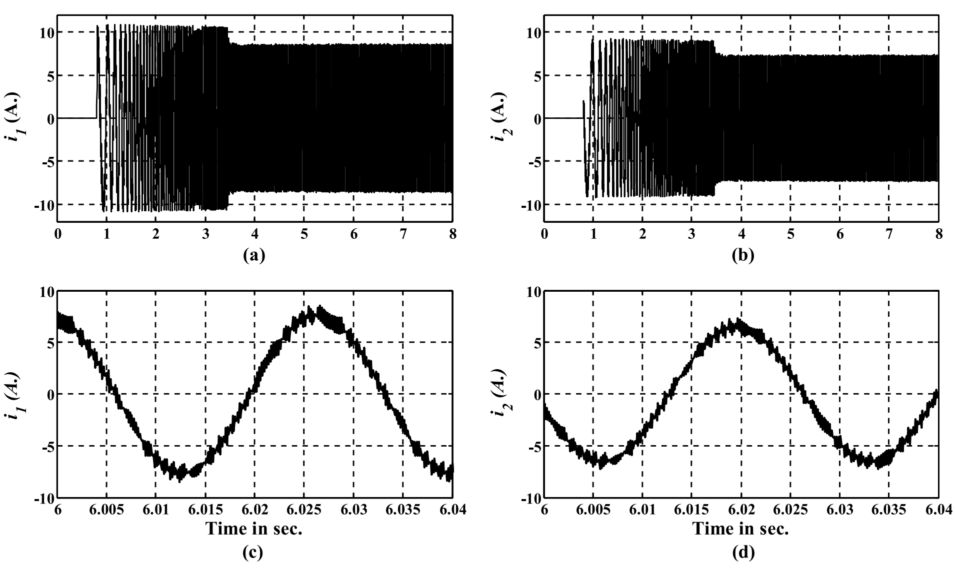

Figure 11. Simulation results of transient and steady-state behavior of the PV array output voltage and current, voltage of the DC filter capacitor, and motor speed at 30% insolation: (a) current in the main winding, (b) current in the auxiliary winding, (c) magnified view of (a), and (d) magnified view of (b).

7. Maximum Power Tracking

Directly coupling a load to the PV array results in a mere utilization of the 31% capacity of the PV array [20]. Hence, in order to make the system more economically competitive, a MPP tracker (MPPT) is employed to ensure that the PV array is always operating at the MPP [21, 22]. It has been shown that MPPTs can extract more than 97% of the PV power when properly optimized [23].

The principle of operation of the MPPT controller is based on the fact that, at each solar insolation level, there is an operating point that yields maximum power extraction. Figure 12 shows the block diagram of the proposed drive system with a MPPT. The MPPT is achieved by placing a boost DC-DC converter. The turn ON/OFF duration of the power transistor of the boost converter is determined by the MPPT controller.

In Section 5, the number of series and parallel PV modules needed to power the proposed system for 8 hr/day were determined. At peak solar insolation, the energy extracted from the PV array at the MPP exceeds what the load requires. In this case, the extra energy at the output of the MPPT is stored in the battery bank. When, on the other hand, the energy extracted from the PV array is less than what the load needs, the stored energy from the battery bank complements the PV energy. In worst-case conditions, when the battery charge is totally depleted, it is shown that the system can run at 70% of its rated power when the solar insolation becomes as low as 30% of the peak value (see Figures 10 and 11).

Various search algorithms have been reported for the operation of the MPPT [24–26]. One of the most popular techniques is the perturb-and-observe (PO) search algorithm, due to its simplicity and ease of implementation. In this algorithm, the voltage and current at the output of the DC-DC converter are measured, and the output power of the converter is calculated. Then, the output voltage of the DC-DC converter is perturbed by a small increment, and the resulting change of power, ΔP, is calculated. If ΔP is positive, then it is supposed that it has moved the operating point closer to the MPP. Thus, further voltage perturbations in the same direction should move the operating point toward the MPP. If, on the other hand, if ΔP is negative, then the operating point must have moved away from the MPP, and the direction of perturbation should be reversed to move back toward the MPP.

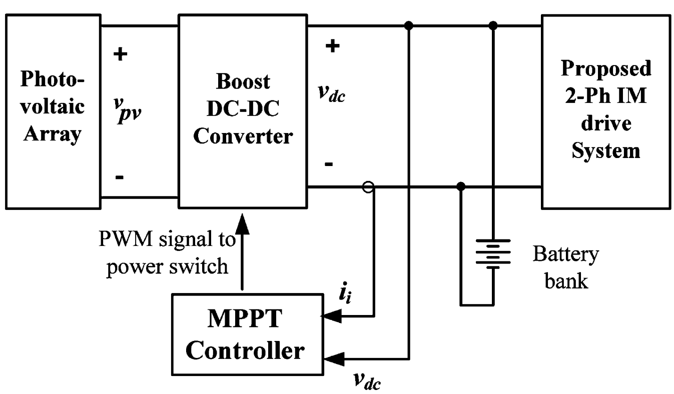

Figure 12. Proposed system with MPPT control.

8. Conclusions

This article presents a new cost-effective control scheme to drive a PV-powered air conditioner with a two-phase IM. Cost-effectiveness is achieved by minimizing the initial and running costs by:

(i) dispensing with the need to manufacture specially designed two-phase IMs and operating a one-phase IM in a more efficient two-phase mode of operation,
(ii) reducing the size of the PV arrays through limiting the motor current during both transient and dynamic stages to 1.5 times its full load value,
(iii) maximizing the use of the available solar radiation by tracking the maximum power line of the PV array, and
(iv) minimizing the running cost by keeping the motor slip at a small value at various operating conditions.

This reduction in the cost/kWh renders the PV system more economically competitive with conventional energy sources. In addition, the proposed system is compact in size.

Simulation results indicate that the control scheme is capable of limiting the motor starting current to 1.5 times its full-load value, yielding sinusoidal motor line current with reduced harmonic content and allowing good transient and dynamic responses of the proposed system.

References

1. Abdel-Rahim, N., and Shaltout, A., "Operation of single-phase Motor as two-phase motor," *Proceedings of the 28th Annual Conference of the IEEE Industrial Electronics Society (IECON)*, pp. 967–972, Sevilla, Spain, 5–8 November 2002.
2. "European Renewable Energy Council, May 2004," available at: http://www.erec.org/documents/publications/2040-scenario.html.
3. Maycock, P. D., "PV review: World solar PV market continues explosive growth," *Refocus*, Vol. 6, No. 5, pp. 18–22, September/October 2005.
4. Li, Q., and Wolfs, P., "A review of the single phase photovoltaic module integrated converter topologies with three different DC link configurations," *IEEE Trans. Power Electron.*, Vol. 23, No. 3, pp. 1320–1333, May 2008.
5. Ren, H., Gao, W., and Ruan, Y., "Economic optimization and sensitivity analysis of photovoltaic system in residential buildings," *Renew. Energy*, Vol. 34, No. 3, pp. 883–889, March 2009.
6. Prasad, B. S., Jain, S., and Agarwal, V., "Universal single-stage grid-connected inverter," *IEEE Trans. Energy Conversion*, Vol. 23, No. 1, pp. 128–137, March 2008.
7. Ordenes, M., Marinoski, D. L., Braun, P., and Rüther, R., "The impact of building-integrated photovoltaics on the energy demand of multi-family dwellings in Brazil," *Energy Buildings*, Vol. 39, No. 6, pp. 629–642, June 2007.
8. Lujara, N. K., Van Wyk, J. D., and Materu, P. N., "Modeling photovoltaic water pumping systems," *Int. J. Renew. Energy Eng.*, Vol. 2, No. 3, pp. 200–213, December 2000.
9. Matsui, K., Yamamoto, I., Hirose, S., Ando, K., and Kobayashi, T. "Utility-interactive photovoltaic power conditioning systems with forward converter for domestic applications," *IEE Proc. Elect. Power Appl.*, Vol. 147, No. 3, pp. 199–205, May 2000
10. Huang, Y., Shen, M., Peng, F. Z., and Wang, J., "Z-source inverter for residential photovoltaic systems," *IEEE Trans. Power Electron.*, Vol. 21, No. 6, pp. 1776–1782, November 2006.
11. Chiang, S. J., Chang, K. T., and Yen, C. Y., "Residential photovoltaic energy storage system," *IEEE Trans. Industrial Electron.*, Vol. 45, No. 3, pp. 385–394, June 1998.

12. Holmes, D. G., and Kotsopoulos, A., "Variable speed control of single-phase and two-phase induction motors using a three-phase voltage source inverter," *IEEE IAS*, Vol. 1, pp. 613–620, 1993.
13. Abdel-Rahim, N., and Shaltout, A., "Unsymmetrical two-phase induction motor drive with slip-frequency control," *IEEE Trans. Energy Conversion*, Vol. 24, No.3, pp. 608–616, September 2009.
14. Krishnan, R., *Electric Motor Drives: Modeling, Analysis and Control*, Upper Saddle River, NJ: Prentice Hall, p. 350, 2001.
15. innovationhouse.com, "Siemens SP75/SP70 Solar Panels," available at: http://www.innovationhouse.com/products/solar_siemens_sp75_sp70.html.
16. Hingorani, N. G., and Gyugyi, L., *Understanding FACTS: Concepts and Technology of Flexible AC Transmission Systems*, New York: IEEE Press, 2000.
17. Markvart, T., *Solar Electricity*, New York: John Wiley and Sons, 2000.
18. The MathWorks Inc., "MATLAB," Natick, MA, 2009, available at: http://www.mathworks.com/.
19. Dewan, S. B., Slemon, G. R., and Straughen, A., *Power Semiconductor Drives*, New York: John Wiley and Sons, p. 7, 1984.
20. Hussein, K. H., Muta, I., Hoshino, T., and Osakada, M., "Maximum photovoltaic power tracking: An algorithm for rapidly changing atmospheric conditions," *IEE Proc. Generat. Transm. Distrib.*, Vol. 142, pp. 59–64, January 1995.
21. Chung, H., Tse, K., Hui, S., Mok, C., and Ho, M., "A novel maximum power point tracking for solar panels using a SEPIC or Cuk converter," *IEEE Trans. Power Electron.*, Vol. 18, No. 3, pp. 717–724, May 2003.
22. Tokushima, D., Uchida, M., Kanbei, S., Ishikawa, H., and Naitoh, H., "A new MPPT control for photovoltaic panels by instantaneous maximum power point tracking," *Elect. Eng. Japan*, Vol. 157, No. 3, pp. 73–80, 2006.
23. Hohm, D. P., and Ropp, M. E., "Comparative study of maximum power point tracking algorithms," *Progress Photovoltaics Res. Appl.*, Vol. 11, No. 1, pp. 47–62, November 2002.
24. Hsieh, G.-C., Chen, H.-L., Chen, Y., Tsai, C.-M., and Shyu, S.-S., "Variable frequency controlled incremental conductance derived MPPT photovoltaic stand-along DC bus system," *23rd Annual IEEE Applied Power Electronics Conference and Exposition (APEC)*, pp. 1849–1854, Austin, TX, 24–28 February 2008.
25. Femia, N., Petrone, G., Spagnuolo, G., and Vitelli, M., "Optimization of perturb and observe maximum power point tracking method," *IEEE Trans. Power Electron.*, Vol. 20, No. 4, pp. 963–973, July 2005.
26. Fermia, N., Granozio, D., Petrone, G., and Vitelli, M., "Predictive & adaptive MPPT perturb and observe method," *IEEE Trans. Aerospace Electron. Syst.*, Vol. 43, No. 3, pp. 934–950, July 2007.

Appendix A. One-phase IM Parameters

1.5 hp, 220 V (RMS), 6 poles
$X_{md} = X_{mq} = 105\ \Omega$
$a = N_1/N_2 = 1/1.18$
$X_1 = 2.01\ \Omega$
$r_1 = 1.3\ \Omega$
$X_2 = 2.8\ \Omega$
$r_2 = 2.6\ \Omega$
$X_{lr} = X_2$
$r_r = 2.01\ \Omega$
$P_{core} = 175$ W
$P_{(friction+windage)} = 75$ W

Appendix B. PV Module Data

Assuming a PSH of 5.5 kWh/m^2 for Siemens solar modules SP75, the following parameters were obtained:

$P_{\max} = 75$ watts, module short circuit current (I_{mod}) $= 4.8$ A,
$I_o = 3.0798 \times 10^{-10}$ A
$\Lambda_c = 39.358$
$R_s = 0.01\ \Omega$
Number of PV cells/module = 36
Module open circuit voltage = 21.7 V

Appendix C. DC Filter Parameters

$L_f = 1.0$ mH
$C_f = 10000.0\ \mu$F
$R_f = 0.1\ \Omega$